



Exchange flows in axially rotating pipes

S. Lyu, M. Izadi , and S. M. Taghavi 

Department of Chemical Engineering, Université Laval, Québec, Québec, Canada G1V 0A6



(Received 5 April 2020; accepted 23 June 2020; published 9 July 2020)

The effects of a pipe axial rotation on buoyant miscible exchange flows are studied experimentally and numerically. The pipe is inclined at intermediate angles, where buoyant and inertial effects are present. The pipe inclination angle and the common viscosity of the fluids are found to have negligible effects on the dynamics of the flow. On the other hand, the pipe rotation speed and the density difference are important flow parameters. The flow is shown to be mainly governed by a balance between the characteristic inertial-buoyant (\hat{V}_i) and rotational (\hat{V}_ω) velocities. By increasing the pipe rotation speed ($\hat{\omega}$), the penetration velocity of the heavy fluid into the light one (\hat{V}_f) decreases and, eventually, the penetration stops at a propagation distance (\hat{L}) within a propagation time period (\hat{T}). It is found that \hat{V}_f , \hat{L} , and \hat{T} decrease nonlinearly with $\hat{\omega}$, and empirical correlations are proposed to predict them versus \hat{V}_ω and \hat{V}_i .

DOI: [10.1103/PhysRevFluids.5.074801](https://doi.org/10.1103/PhysRevFluids.5.074801)

I. INTRODUCTION

Buoyancy-driven stratified flows are ubiquitous in nature and industry, and they have been extensively investigated for different flow problems [1–3]. In confined geometries, buoyant miscible lock-exchange flows have been studied experimentally and numerically, in vertical [4–6], inclined [7,8], and near-horizontal [9,10] pipes. In this work, we experimentally and numerically analyze the effects of a pipe axial rotation on buoyant miscible flows, in a lock-exchange configuration in an inclined pipe.

The previous studies of miscible exchange flows have been almost entirely in static flow geometries, focusing on quantifying the penetration velocities of the heavy fluid into the light one, \hat{V}_f . For example, the experimental study of Séon *et al.* [11] has reported that \hat{V}_f is independent of the inclination angle with respect to vertical, β , over the range of $65^\circ < \beta < 82^\circ$. They have argued that the flow dynamics, in particular the front velocity, is governed by a balance between inertia and buoyancy, resulting in $\hat{V}_f \approx \sqrt{At\hat{g}\hat{R}}$, where \hat{R} is the pipe radius, \hat{g} is the gravitational acceleration, and At is the Atwood number, i.e., the ratio of the density difference to the density summation.

Although exchange flows in rotating flow geometries have not been studied, there are several works in the literature on the stability of a single fluid flowing in a rotating pipe [12–14], revealing that the pipe rotation changes the basic nature of the flow stability. For instance, the pioneering theoretical work of Pedley [12] has provided a criterion to roughly estimate the transition between stable and unstable flows, based on the flow Reynolds number, while more recent studies have experimentally analyzed convective and absolute instabilities of the Hagen-Poiseuille flow in rotating pipes [15,16]. In addition to these types of works, there are also studies on the Rayleigh-Taylor instabilities in rotating cylinders, especially thanks to the recent discovery of the inhabitation of these instabilities using rotational motion [17].

*Seyed-Mohammad.Taghavi@gch.ulaval.ca

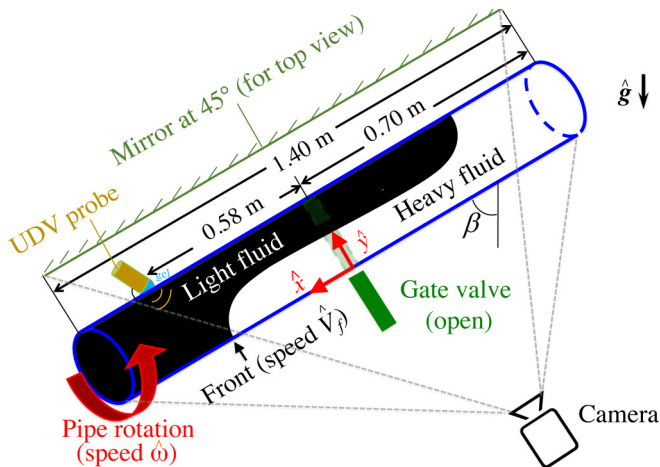


FIG. 1. A schematic view of the experimental setup. The interface shape is illustrative only.

There are a few studies on buoyant miscible flows in rotating flow geometries, mainly in the context of displacement flows in pipes and annuli. For instance, Carrasco and Frigaard [18] have demonstrated that an inner cylinder rotation in annular miscible displacements causes the heavy fluid to be positioned above the light one at certain azimuthal conditions, which may lead to buoyancy-driven fingering. Lyu and Taghavi [19] have studied buoyant miscible displacement flows in axially rotating pipes, finding that a complete removal of the displaced fluid by the displacing fluid can be achieved when the pipe rotation speed exceeds a critical value. Above the critical condition, they have found that the penetration velocity of the heavy fluid into the light fluid, \hat{V}_f , is proportional to the mean imposed displacement velocity \hat{V}_0 , following $\hat{V}_f \approx 1.3\hat{V}_0$.

The current paper investigates experimentally and numerically buoyant miscible exchange flows in an axially rotating pipe. Some of the novelties of our study are as follows. (1) We are aware of no other experimental or numerical study of exchange flows in rotating flow geometries. (2) Distinct flow behaviors in a rotating pipe are identified and they are found to be completely different from those in a static pipe. (3) The effects of the pipe rotation on the flow dynamics are studied; in particular, the penetration front velocity, which is one of the key characteristics of exchange flows, is quantified versus the pipe rotation speed.

The paper is organized as follows. In Sec. II, the experimental setup is described briefly, and in Sec. III the experimental results are presented. The latter initially presents the general effects of a pipe rotation on exchange flows in an inclined pipe. Then, the effects of the flow parameters, e.g., the inclination angle, the density difference, the pipe rotation speed, and the common viscosity of the fluids, on the penetration front velocity are quantified. In Sec. IV, numerical results are presented to gain better insight into the flow dynamics. In Sec. V, the main findings are briefly summarized.

II. EXPERIMENTAL METHOD

This study investigates the exchange flow behavior of two Newtonian fluids interpenetrating into each other, in a density-unstable configuration, in an axially rotating pipe. The pipe is inclined at intermediate inclination angles. The fluids are miscible, they have a small density difference (in the Boussinesq approximation limit), and they have nearly equal kinematic viscosities (i.e., small). The pipe radius is much smaller than its length; i.e., the pipe has a large aspect ratio.

The experiments are performed in a transparent (acrylic) pipe (with the inner radius of $\hat{R} = 9.53$ mm) that is mounted on a robust frame. The pipe is inclined at angle β from vertical. Figure 1 depicts a schematic of the experimental setup and Table I provides the flow parameter ranges in this

TABLE I. Flow parameters and their ranges in this study.

Parameter	Description	Range
β	Pipe inclination angle from vertical	65,68,70,75,76.1,80 degrees
$\hat{\nu}$	Common kinematic viscosity	1,1.8,2.5 mm ² /s
At	Atwood number	$(1.5 \pm 0.3, 5.5 \pm 0.3, 10 \pm 1) \times 10^{-3}$
$\hat{\omega}$	Angular frequency of rotation	0–7.33 rad/s

study. The pipe (with the length of 140 cm) is divided into two equal parts (each with the length of 70 cm) by an automated pneumatic gate valve. Stable pipe rotations around the pipe symmetry axis are powered by a stepper motor and controlled by a custom written LabView program, producing a precise rotation speed ($\hat{\omega}$), over $\sim 10^{-3}$ s to reach steady state. Six vertical supports are installed on the setup so that any pipe vibrations or fluctuations remain below 10^{-1} mm, even at high rotation speeds.

A high-resolution digital camera (Basler acA2040, 2^{12} gray-scale levels) covering the whole pipe length is used to acquire images at 5 frames per second. The pipe is backlit using light-emitting diode (LED) strips placed behind diffusive layers to improve light homogeneity. A set of first surface mirrors is installed in parallel with the pipe axis, to obtain top view images from the pipe.

Sodium chloride (Sigma-Aldrich, assay $\geq 99\%$) as a weighting agent is added to pure water to make the heavy fluid. This results in achieving a small Atwood number, $At = (\hat{\rho}_H - \hat{\rho}_L)/(\hat{\rho}_H + \hat{\rho}_L)$, where $\hat{\rho}_H$ and $\hat{\rho}_L$ are the densities of the heavy and light fluids, respectively. A small amount of ink (Fountain Pen India, 650 mg/L) is added to pure water to prepare the lighter fluid. The kinematic viscosities are altered by adding pure glycerin to both fluids in certain experiments. The density and viscosity of the fluids are measured by a high-precision density meter (Anton Paar DMA 35) and a rheometer (DHR-3, TA Instruments), respectively. All the experiments are performed at an ambient temperature kept at 22 ± 1 °C. Table I lists the flow parameters and their ranges in our experiments.

To gain additional insight into the flow dynamics, an ultrasonic Doppler velocimeter (UDV-DOP4000, Signal Processing SA) is employed to acquire local axial velocity profiles across the pipe. The measurements are made at 54 cm downstream of the gate valve. The UDV probe is mounted at an angle $\approx 70^\circ$ relative to the axis of the pipe, to have a good signal-to-noise ratio [20]. For the tracer, a volumetric seeding particle concentration of 0.2 g/L is used in the UDV measurements.

III. EXPERIMENTAL RESULTS AND DISCUSSION

In a density-unstable exchange flow in an inclined pipe, the heavy fluid slumps underneath the lighter fluid, as depicted schematically in Fig. 1. Two fronts can be observed in an exchange flow in a static pipe. The heavy fluid front (toward the lower wall), with velocity \hat{V}_f , and the light fluid front (toward the upper wall), with nearly the same velocity as the heavy fluid front, propagate in opposite directions. Our experiments focus on analyzing the effects of a pipe axial rotation on this exchange flow configuration.

A. General flow behaviors

Figure 2 shows the development of the exchange flow patterns with increasing pipe rotation speeds. The concentration values are normalized so they vary between 0 and 1, throughout the paper. The flow has a 2-fold rotational symmetry with respect to the middle point of the gate valve, so only the lower part of the gate valve is shown. When there is no pipe rotation [see Figs. 2(a) and 2(e) for the side and top view images, respectively], the flow dynamics is mainly governed by buoyancy. The buoyant stress is on the order of $At\hat{g}\hat{R}$, resulting in the interpenetration of the two fluids; the heavy fluid front advances downward and the light fluid front moves upward. The transverse component of buoyancy, on the other hand, keeps the heavy and light fluids segregated and avoids efficient

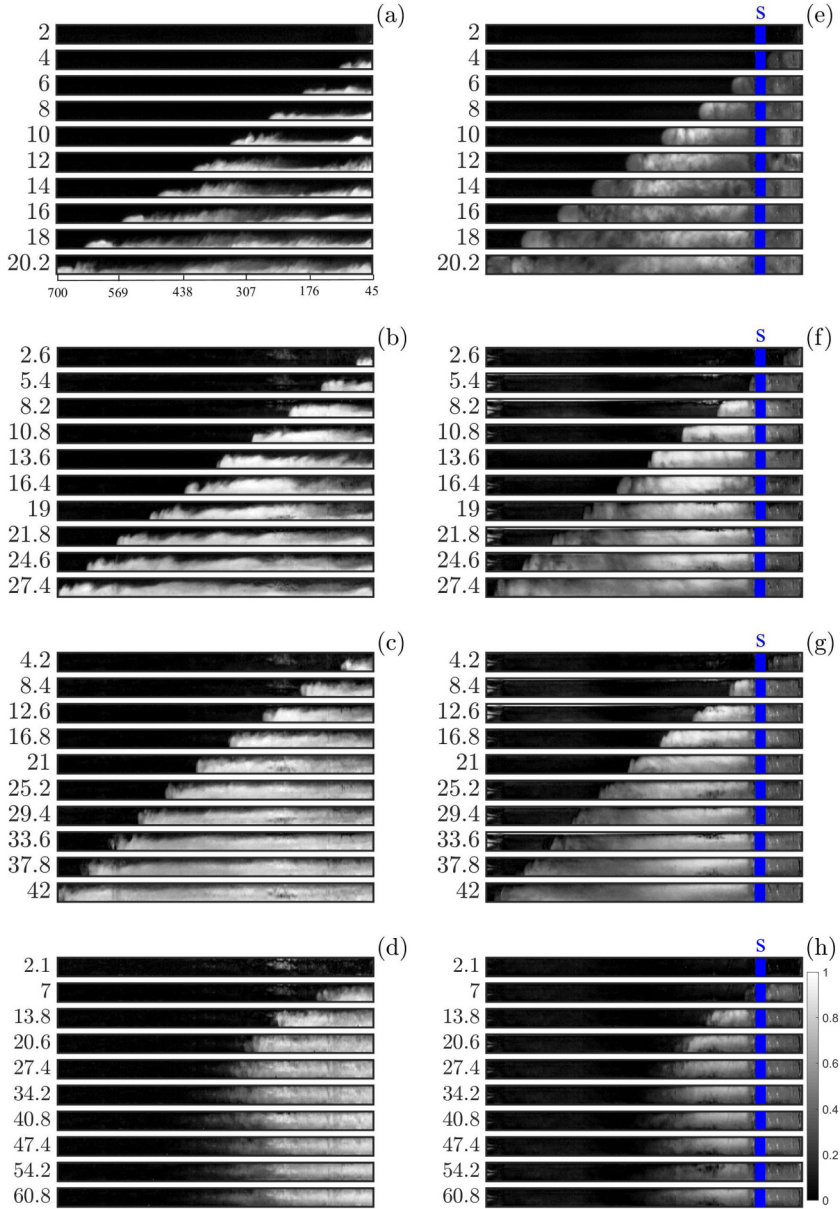


FIG. 2. (a)–(d) Sequence of experimental snapshots at $\beta = 75^\circ$, $\hat{\nu} = 1 \text{ mm}^2/\text{s}$, and $At = 10^{-2}$, with increasing rotation speed: (a) $\hat{\omega} = 0$, (b) $\hat{\omega} = 2.09$, (c) $\hat{\omega} = 3.14$, and (d) $\hat{\omega} = 4.19 \text{ rad/s}$. The corresponding top view images are shown in panels (e) to (h). Experimental times in seconds, \hat{t} , are indicated beside each snapshot, here and elsewhere. The field of view in each snapshot is $19 \times 655 \text{ mm}^2$, 45 mm below the gate valve. The heavy fluid moves from right to left in each snapshot. The mirror support is marked by the blue S. The \hat{x} -axis scale label in panel (a) corresponds to all the panels and indicates the distance from the gate valve in millimeters.

transverse mixing. Although the interface between the heavy and light fluids looks unstable and billow-like waves appear at the interface, they do not contribute to a strong mixing zone within the duration of the experimental test. By introducing a small rotation speed, i.e., $\hat{\omega} = 2.09 \text{ rad/s}$ in



FIG. 3. Front shape images at $\beta = 75^\circ$, $\hat{v} = 1 \text{ mm}^2/\text{s}$, and $At = 10^{-2}$, with increasing rotation speed (a)–(d): $\hat{\omega} = 0, 1.05, 2.09$, and 3.14 rad/s . The photos are captured at $\hat{t} = [7.4, 8.6, 10.3, 13.0] \text{ s}$ from top to bottom. The field of view is $19 \times 240 \text{ mm}^2$, 45 mm below the gate valve. The side view of the flow is shown here and throughout the paper, unless otherwise stated.

Figs. 2(b) and 2(f), the rotational inertia starts to play a role in governing the flow behaviors, but it is not sufficiently strong to completely overcome the transverse buoyancy force. Therefore, partial mixing between the fluids is observed, while there is still a thin layer of the light fluid remaining on the pipe upper walls. As the rotational inertia becomes stronger, i.e., $\hat{\omega} = 3.14 \text{ rad/s}$ in Figs. 2(c) and 2(g), it eventually overcomes the transverse buoyancy force that separates the two fluids. As a result, the fluids mix more efficiently in the transverse direction and the light fluid layer becomes much thinner. However, even with the mixing present between the fluids, the mixture maintains a density difference that is sufficient to drive the front to move forward. At a higher rotation speed, i.e., $\hat{\omega} = 4.19 \text{ rad/s}$ in Figs. 2(d) and 2(h), the fluids become sufficiently mixed; consequently, the buoyancy force significantly decreases and the front eventually begins to be nearly motionless after a propagation distance. Comparing Figs. 2(d) and 2(h) reveals that, at a high rotation speed, the side and top view images are very similar, implying that the mixing becomes efficient and the flow becomes nearly symmetric with respect to the pipe axis.

Figure 3 provides a closer look at the variation of the interface for increasing values of the rotation speed, showing the effects of the rotation speed on the front shape. By increasing the rotation speed the penetration front shape progressively changes.

For typical flow parameters and for increasing values of the rotation speed, examples of flow spatiotemporal diagrams of the depth-averaged concentration are shown in Fig. 4. In a static pipe, a sharply propagating front can be observed on the spatiotemporal diagram of Fig. 4(a). The front velocity \hat{V}_f can be quantified by the slope of the line that separates the black and gray regions in the diagram. Behind the front, certain interfacial waves appear and they seem to propagate against the heavy fluid flow direction. When the rotation speed gradually increases, i.e., $\hat{\omega} = 1.05 \text{ rad/s}$ in Fig. 4(b), the front velocity decreases. When the rotation speed is increased to $\hat{\omega} = 2.62 \text{ rad/s}$ in Fig. 4(c), \hat{V}_f further decreases. For $\hat{\omega} > 2.62 \text{ rad/s}$ in Figs. 4(d)–4(h), the penetration front practically stops somewhere downstream, at a propagation distance with respect to the gate valve. As shown in Fig. 4, the value of the propagation distance slowly decreases with increasing rotation speed.

In this work, the exchange flows for which the penetration front stops are called nearly stagnant flows. Here, the term “nearly” is necessary since the two pure fluids are separated by a mixed zone and the longitudinal mixing can still be macroscopically diffusive. In fact, through fitting a solution of the classical diffusion equation onto the mean concentration profiles, a macroscopic diffusion coefficient of $O(10^{-4}) \text{ m}^2/\text{s}$ for these flows can be very crudely obtained (depending on $\hat{\omega}$).

B. Velocity profiles

Figure 5 illustrates the contours of the local axial velocity component in mm/s in the plane of \hat{i} and \hat{j} , corresponding to the experiments in Figs. 4(a)–4(c). The axial velocity profiles are recorded as soon as the gate valve is opened. As the UDV probe is placed at $\hat{x} = 54 \text{ cm}$, it takes some time for the exchange flow to reach its position. It can be seen in Fig. 5(a) that the lower part of the

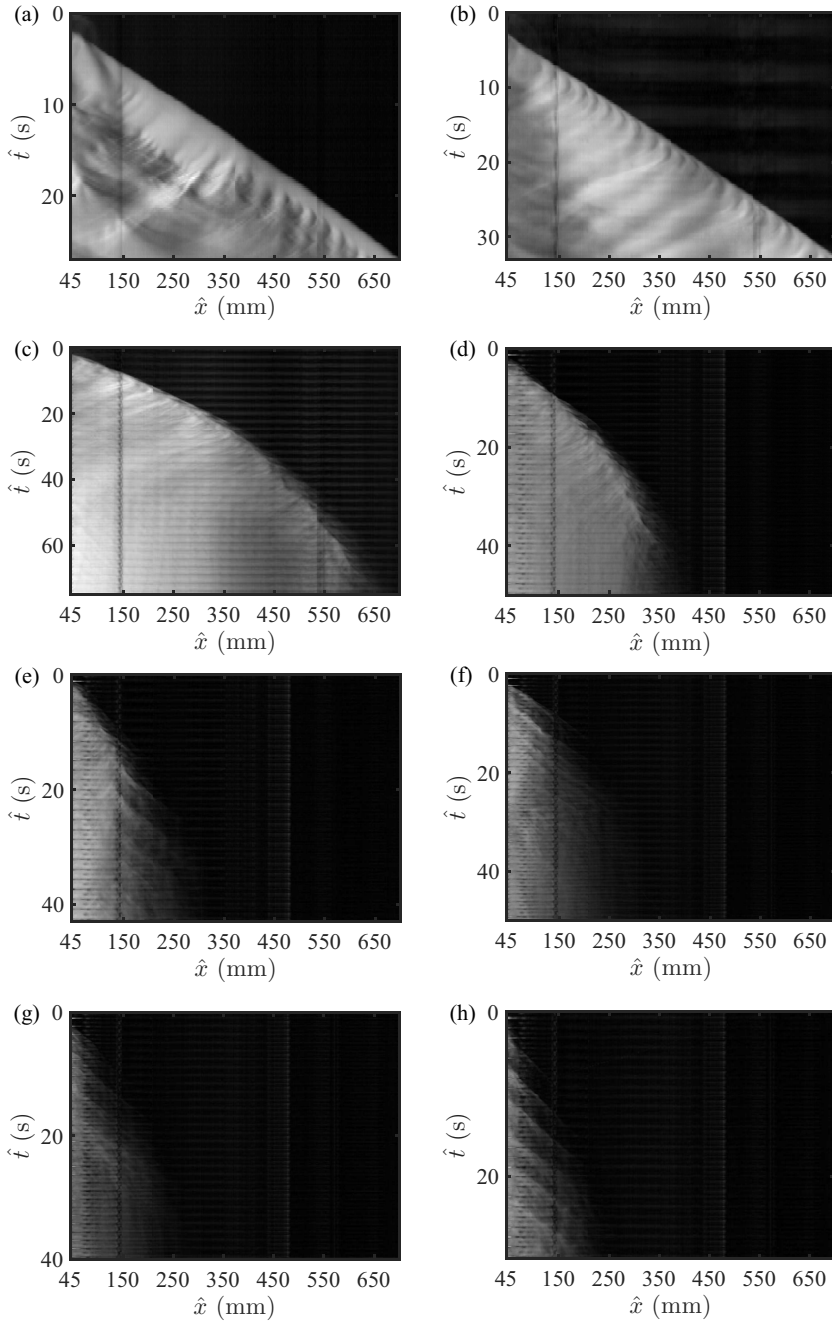


FIG. 4. Spatiotemporal diagrams at $\beta = 75^\circ$, $\hat{v} = 1 \text{ mm}^2/\text{s}$, and $At = 5.5 \times 10^{-3}$ with increasing pipe rotation speeds: (a) $\hat{\omega} = 0$, (b) $\hat{\omega} = 1.05$, (c) $\hat{\omega} = 2.62$, (d) $\hat{\omega} = 3.14$, (e) $\hat{\omega} = 3.67$, (f) $\hat{\omega} = 4.19$, (g) $\hat{\omega} = 4.71$, and (h) $\hat{\omega} = 5.24 \text{ rad/s}$.

axial velocity profile has positive values while the upper part shows negative values, indicating a countercurrent flow. Figure 5(b) shows that, by increasing the rotation speed, the axial velocity

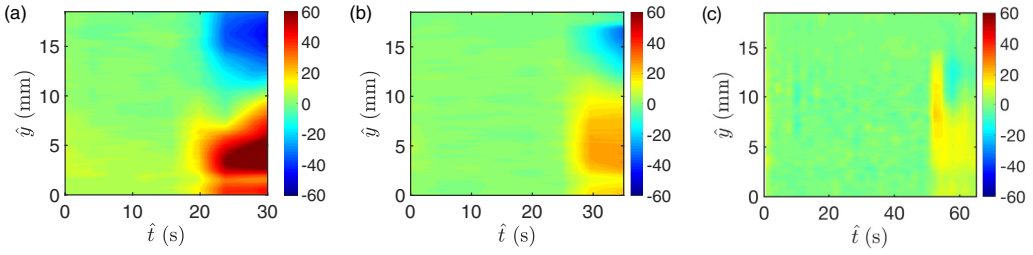


FIG. 5. Contours of the local axial velocity component in mm/s versus \hat{t} and \hat{y} , corresponding to the experiments of panels (a)–(c) in Fig. 4.

component decreases. Finally, the velocity field in Fig. 5(c) corresponds to a slowly moving mixing zone at a higher rotation speed.

To investigate the local axial velocity characteristics, for low and moderate rotation speeds, Fig. 6 is plotted. Figures 6(a) and 6(b) depict experimental images at five different times, for $\hat{\omega} = 1.05$ rad/s and $\hat{\omega} = 2.62$ rad/s, respectively. On these images, the vertical blue line marks the position

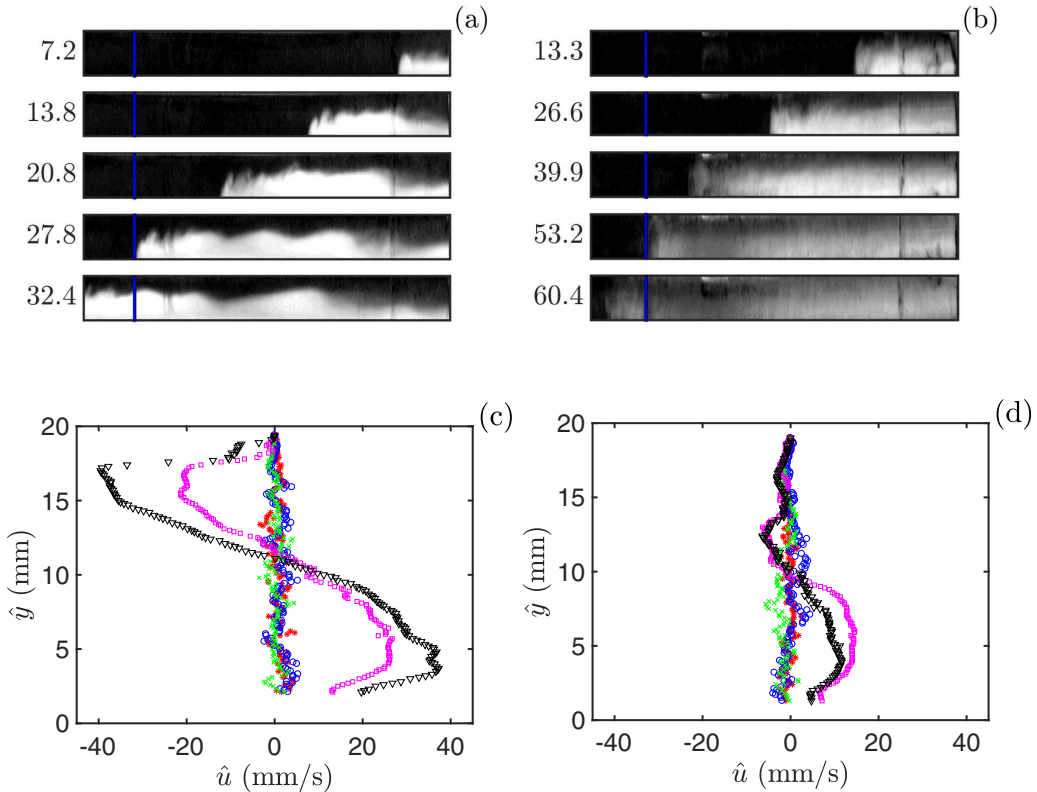


FIG. 6. (a), (b) Experimental snapshots for $\beta = 75^\circ$, $\hat{v} = 1 \text{ mm}^2/\text{s}$, and $At = 5.5 \times 10^{-3}$ at (a) $\hat{\omega} = 1.05$ rad/s and (b) $\hat{\omega} = 2.62$ rad/s. The field of view is $19 \times 655 \text{ mm}^2$, 45 mm below the gate valve (the images are stretched vertically for a better visualization). The location where the local velocity profile is recorded is marked by the vertical blue line. (c), (d) The velocity profiles corresponding roughly to panels (a) and (b), from top to bottom, with the following symbols: red *, blue \circ , green \times , purple \square , and black ∇ . Close to the lower wall, there are UDV instrumental errors so the velocities close to the lower wall are removed.

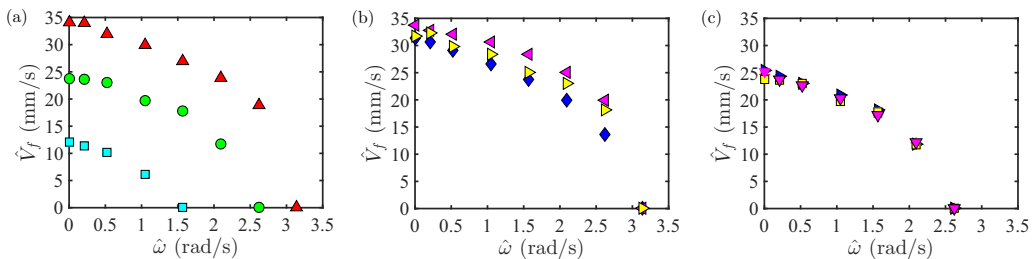


FIG. 7. The variation of the front velocity, \hat{V}_f , as a function of the rotation speed, $\hat{\omega}$, for (a) $\beta = 75^\circ$, $\hat{\nu} = 1 \text{ mm}^2/\text{s}$, and different density contrasts: $At = 10^{-2}$ (red \blacktriangle), $At = 5.5 \times 10^{-3}$ (green \bullet), and $At = 1.5 \times 10^{-3}$ (cyan \blacksquare); (b) $\beta = 75^\circ$, $At = 10^{-2}$, and different viscosities: $\hat{\nu} = 1 \text{ mm}^2/\text{s}$ (blue \blacklozenge), $\hat{\nu} = 1.8 \text{ mm}^2/\text{s}$ (magenta \blacktriangleleft), $\hat{\nu} = 2.5 \text{ mm}^2/\text{s}$ (yellow \blacktriangleright); (c) $At = 5.5 \times 10^{-3}$, $\hat{\nu} = 1 \text{ mm}^2/\text{s}$, and different inclination angles: $\beta = 65^\circ$ (red $*$), $\beta = 68^\circ$ (green \cdot), $\beta = 70^\circ$ (blue \blacktriangleright), $\beta = 75^\circ$ (yellow \blacksquare), and $\beta = 80^\circ$ (magenta \blacktriangledown).

of the UDV probe where the axial velocity profiles are measured. For the first three snapshots from the top in Figs. 6(a) and 6(b), the axial velocity profiles are nearly zero; i.e., there is no flow motion in the axial direction (note that the velocity fluctuations are due to inevitable experimental noise). In the fourth snapshots from the top in Figs. 6(a) and 6(b), the front approximately reaches the position of the UDV probe. In the last snapshots from the top in Figs. 6(a) and 6(b), the front has passed the position of the UDV probe. The axial components of the velocity profile across the pipe are plotted in Figs. 6(c) and 6(d), which correspond to Figs. 6(a) and 6(b), respectively. Figure 6(c) plots the velocity profiles at a low rotation speed, showing that, initially, the light fluid does not move in the axial direction before the front reaches the UDV probe position. When the front reaches the UDV probe position, a countercurrent flow appears: the heavy fluid moves downstream while the lighter fluid is pushed upward. At longer times when the front has completely passed the UDV probe position, the countercurrent flow is enhanced. Figure 6(d) shows the velocity profiles at a higher rotation speed. Initially, the light fluid does not move. At longer times, when the front reaches and passes the UDV probe position, the velocity profiles correspond to a mixing zone.

C. Front velocity

Figure 7 shows the variations of the long-time front velocity, \hat{V}_f , as a function of the rotation speed, $\hat{\omega}$, for different flow parameters, i.e., the density difference [Fig. 7(a)], the kinematic viscosity [Fig. 7(b)], and the pipe inclination angle [Fig. 7(c)]. In Fig. 7(a), the pipe inclination angle is fixed at $\beta = 75^\circ$, the viscosity is fixed at $\hat{\nu} = 1 \text{ mm}^2/\text{s}$, and the results for three Atwood numbers, i.e., $At = 10^{-2}$, 5.5×10^{-3} , and 1.5×10^{-3} , are shown. By increasing the Atwood number, the front velocity increases, as expected. By increasing the pipe rotation speed, on the other hand, for a fixed Atwood number the front velocity gradually decreases, reaching zero at higher rotation speeds. The critical rotation speed for which the front velocity becomes nearly zero depends on the Atwood number; beyond the critical rotation speed, the front velocity remains to be zero (results omitted for brevity). Figure 7(b) shows \hat{V}_f versus $\hat{\omega}$, for fixed $\beta = 75^\circ$ and $At = 10^{-2}$; the common kinematic viscosity of the fluids varies in the range of $\hat{\nu} = 1\text{--}2.5 \text{ mm}^2/\text{s}$. As can be seen, increasing the viscosity of the fluids does not have an effect as significant as that of increasing the density difference or the rotation speed; thus, relatively speaking, we can assume that the values of \hat{V}_f for different $\hat{\omega}$ do not much depend on $\hat{\nu}$ (in other words, relative to the other critical flow parameters, we may ignore the effects of viscous dissipation on the flow when $\hat{\nu}$ is kept small). Figure 7(c) also shows that the variation of the front velocity versus the pipe rotation speed is independent of the pipe inclination angles.

The gradual decrease of \hat{V}_f with increasing $\hat{\omega}$ can be mainly attributed to the effect of the pipe rotation on the degree of mixing between the two fluids. When the rotational inertia overcomes the

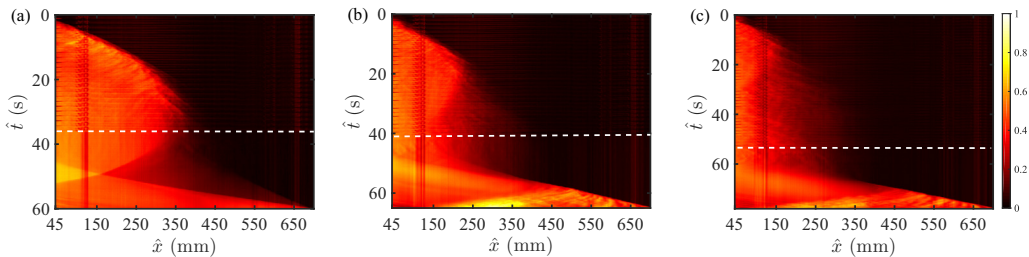


FIG. 8. Spatiotemporal diagrams at $\beta = 76.1^\circ$, $\hat{\nu} = 1 \text{ mm}^2/\text{s}$, and $At = 10^{-2}$ with increasing pipe rotation speeds: $\hat{\omega} =$ (a) 4.19, (b) 4.71, and (c) 5.24 rad/s. The white horizontal dashed lines indicate the time when the pipe rotation stops.

transverse buoyancy, the fluids mix and the buoyancy force decreases, depending on the degree of mixing between the fluids. This mixing contributes to decreasing the longitudinal buoyancy force that drives the fluids in the axial direction.

Figure 7 shows that \hat{V}_f eventually reaches zero at large values of $\hat{\omega}$, for any value of β , $\hat{\nu}$, and At . Although the significant decrease in \hat{V}_f is due to the mixing induced by the rotation, there seem to be other factors that also contribute to arresting the front, causing \hat{V}_f to reach zero at large $\hat{\omega}$. For instance, Fig. 2(d) and Figs. 4(e)–4(h) clearly illustrate that distinct density contrasts still persist at the large rotation speed limit. In fact, one may argue that, in the absence of the pipe rotation, such a density difference could be sufficient to induce an exchange flow. To examine this hypothesis, Fig. 8 shows a series of experiments, for a typical parameter set at high rotation speeds (a different color map is used for better visualization). In these experiments, we intentionally stop the pipe rotation at a certain time after the heavy fluid front has stopped propagating. As can be seen, the previously stagnant front becomes remobilized when the pipe rotation stops, confirming that the mixing alone is insufficient to hold the front stagnant. As the remobilization front dynamic is transient and complex, we will leave the deep analysis of this flow to future works.

A conclusion drawn from Fig. 8 is that, although the mixing between the fluids significantly contributes to decreasing the longitudinal buoyant force and thus decreasing the front velocity, this mixing is not sufficient to the degree that the longitudinal buoyancy goes all the way to zero, which, in the absence of the other forces, would be necessary to completely arrest the exchange flow. Thus, it is insightful to attempt to explain (at least qualitatively) why the exchange flow stops at large rotation speeds. First, note that it is known that a rotating fluid can arrange itself into coherent vertical structures aligned with the rotation axis [21]. Therefore, in the axial direction and especially within the mixing zone, there is a competition or balance between the buoyant force (significantly weakened by mixing) and the Coriolis force, at large rotation speeds. The former has a destabilizing effect on the flow, attempting to generate an overturning motion in the mixing zone and cause an interpenetration of the fluids. The latter force, on the other hand, causes a stabilizing effect in the axial direction, particularly by organizing the flow into vertical structures aligned with the pipe rotation axis [22]. In other words, the Coriolis force at large rotation speeds imparts a vertical rigidity to the flow [23] that notably reduces the fluid movement in the pipe radial planes, as a result of the Taylor-Proudman theorem [22,24]; this also hinders velocity gradients parallel to the rotation axis, impeding large-scale overturning of the mixing zone and preventing the fluid layers from bypassing each other in the axial direction. A similar mechanism is observed in the inhibition of the Rayleigh-Taylor instabilities in rotating cylinders [17,21].

Based on our results so far, it can be said that the balance between the rotational inertia and the transverse buoyancy plays an important role in the dynamics of our flows. At zero rotation speed, the transverse buoyancy force can segregate the two-fluid layer, keeping the density contrast large especially near the front, which in return can create adequate longitudinal buoyancy forces to maintain the interpenetration of the two fluids. As the rotation speed increases, the transverse

buoyancy can be overcome by the rotational inertia resulting in transverse mixing, decreasing the local density contrast, which in return weakens the local longitudinal buoyancy for the interpenetration of the two fluids to continue. The buoyancy stress is proportional to $(\hat{\rho}_H - \hat{\rho}_L)\hat{g}\hat{R}/2$, while the rotational inertial stress is proportional to $(\hat{\rho}_H + \hat{\rho}_L)(\hat{\omega}\hat{R})^2/2$, resulting in the following balance,

$$\frac{(\hat{\rho}_H + \hat{\rho}_L)}{2}(\hat{\omega}\hat{R})^2 \sim \frac{(\hat{\rho}_H - \hat{\rho}_L)\hat{g}\hat{R}}{2}, \quad (1)$$

which gives a ratio of

$$\left(\frac{(\hat{\rho}_H + \hat{\rho}_L)(\hat{\omega}\hat{R})^2}{2} \right)^{1/2} \equiv \frac{\hat{\omega}\hat{R}}{\sqrt{At\hat{g}\hat{R}}} \equiv \frac{\hat{V}_\omega}{\hat{V}_i} \quad (2)$$

as the main parameter governing the flow dynamics in our rotating pipe flows. In the equation above, \hat{V}_ω is the pipe circumferential velocity, i.e., the characteristic rotational velocity of the flow system, and \hat{V}_i is the characteristic inertial-buoyant velocity, i.e., obtained by a balance between inertial and buoyant forces. On the other hand, as also shown by [11], the dynamics of the buoyant exchange flow in a static pipe is governed by \hat{V}_i ; for instance, $\hat{V}_f = f(\hat{V}_i)$. Therefore, for the exchange flow front velocity in a rotating pipe, we can simply write

$$\frac{\hat{V}_f}{\hat{V}_i} = f\left(\frac{\hat{V}_\omega}{\hat{V}_i}\right). \quad (3)$$

The analysis so far is consistent with our experimental observations; i.e., \hat{V}_f is independent of the pipe inclination angle as well as the kinematic viscosity of the fluids, but it depends on the density contrast between the fluids as well as the pipe rotation speed. Observing a nonlinear variation of $\frac{\hat{V}_f}{\hat{V}_i}$ versus $\frac{\hat{V}_\omega}{\hat{V}_i}$ in our experiments, we attempt to fit a quadratic function onto our results in the form of

$$\frac{\hat{V}_f}{\hat{V}_i} \approx a_0 + a_1\left(\frac{\hat{V}_\omega}{\hat{V}_i}\right) + a_2\left(\frac{\hat{V}_\omega}{\hat{V}_i}\right)^2. \quad (4)$$

We rescale \hat{V}_f with \hat{V}_i for all our experimental data and fit the coefficients in Eq. (4). We find that $a_0 = 1.07$, $a_1 = -0.24$, and $a_2 = -0.41$ in the confidence interval $a_1 \in (1.06, 1.09)$, $a_2 \in (-0.32, -0.15)$, and $a_3 \in (-0.5, -0.32)$ with confidence level 95%. The coefficient $a_0 = 1.07$ is in excellent agreement with the findings of [11] for a corresponding static pipe flow. Figure 9 shows a comparison of the experimental data with the prediction

$$\frac{\hat{V}_f}{\hat{V}_i} \approx 1.07 - 0.24\left(\frac{\hat{V}_\omega}{\hat{V}_i}\right) - 0.41\left(\frac{\hat{V}_\omega}{\hat{V}_i}\right)^2. \quad (5)$$

The collapse of the data with respect to \hat{V}_ω/\hat{V}_i is evident and the approximation is quite reasonable for smaller values of \hat{V}_ω/\hat{V}_i , e.g., when $\hat{V}_\omega/\hat{V}_i \lesssim 1$. At large \hat{V}_ω/\hat{V}_i , however, correlation (5) is no longer applicable to predicting the front velocity.

D. Front propagation distance

We have observed that at high rotation speeds, the front stops advancing over a distance with respect to the gate valve, which we call the front propagation distance (\hat{L}). Our criterion to quantify this distance where the penetration stops (as well as the time at which it occurs) is a significant decrease in the front velocity, i.e., reaching the value of $\hat{V}_f = 1$ mm/s. Intuitively, \hat{L} decreases with increasing $\hat{\omega}$. Figure 10(a) shows the variation of \hat{L} versus $\hat{\omega}$ for different density contrasts, At , inclination angles, β , and kinematic viscosities, $\hat{\nu}$. The propagation distance decreases dramatically with increasing rotation speed and it eventually reaches a small value at very high rotation speeds.

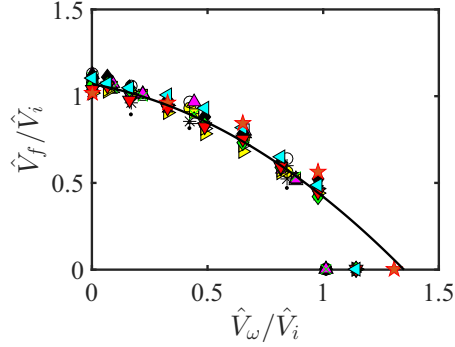


FIG. 9. Dimensionless front velocity, \hat{V}_f/\hat{V}_i , as a function of \hat{V}_ω/\hat{V}_i . The data points correspond to $At = 1.5 \times 10^{-3}$ and $\hat{v} = 1 \text{ mm}^2/\text{s}$ at $\beta = 65^\circ$ (yellow \bullet), $\beta = 68^\circ$ (black \circ), $\beta = 70^\circ$ (magenta $+$), $\beta = 75^\circ$ (blue $*$), and $\beta = 80^\circ$ (green \cdot); $At = 5.5 \times 10^{-3}$ and $\hat{v} = 1 \text{ mm}^2/\text{s}$ at $\beta = 65^\circ$ (yellow \blacksquare), $\beta = 68^\circ$ (black \square), $\beta = 70^\circ$ (magenta \blacktriangle), $\beta = 75^\circ$ (black \triangle), and $\beta = 80^\circ$ (green \times); $At = 10^{-2}$ and $\hat{v} = 1 \text{ mm}^2/\text{s}$ at $\beta = 65^\circ$ (yellow \blacktriangleright), $\beta = 68^\circ$ (black \triangleright), $\beta = 70^\circ$ (magenta \star), $\beta = 75^\circ$ (black \blacklozenge), and $\beta = 80^\circ$ (green \diamond); $At = 10^{-2}$ and $\hat{v} = 1.8 \text{ mm}^2/\text{s}$ at $\beta = 70^\circ$ (red \blacktriangledown); $At = 10^{-2}$ and $\hat{v} = 2.5 \text{ mm}^2/\text{s}$ at $\beta = 70^\circ$ (cyan \blacktriangleleft). The solid line represents the prediction of the empirical correlation (5). Simulation results, described later in the text, are marked by orange \star and correspond to $At = 10^{-2}$, $\hat{v} = 1 \text{ mm}^2/\text{s}$, and $\beta = 75^\circ$.

Figure 10(b) shows the results of Fig. 10(a) plotted in dimensionless form in the plane of $(\hat{V}_\omega/\hat{V}_i, \hat{L}/\hat{R})$. The collapse of the data is not perfect but it is still reasonable to fit a power-law function in the form of

$$\frac{\hat{L}}{\hat{R}} \approx a + b \left(\frac{\hat{V}_\omega}{\hat{V}_i} \right)^c, \quad (6)$$

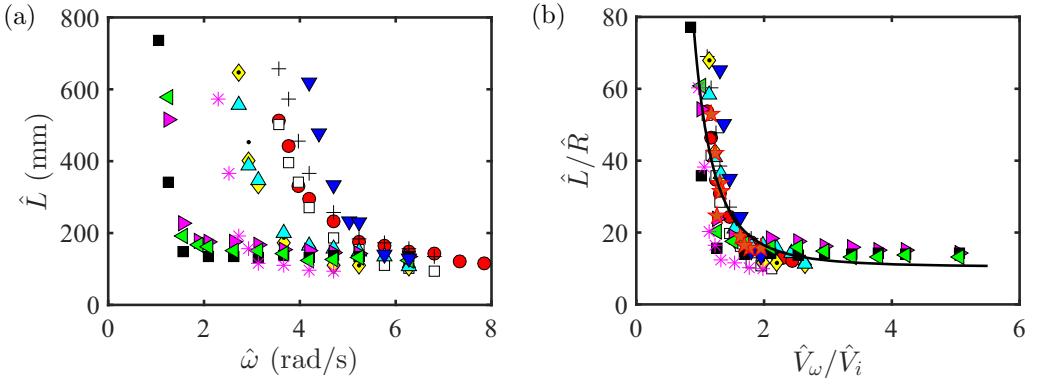


FIG. 10. Variation of the propagation distance of the stopping front as a function of the pipe rotation speed plotted in (a) the dimensional plane $(\hat{\omega}, \hat{L})$; (b) the dimensionless plane $(\hat{V}_\omega/\hat{V}_i, \hat{L}/\hat{R})$. Different markers represent the data points: $At = 10^{-2}$ and $\hat{v} = 1 \text{ mm}^2/\text{s}$ at $\beta = 75^\circ$ (red \bullet), $\beta = 80^\circ$ (black $+$), $\beta = 70^\circ$ (black \square); $At = 5.5 \times 10^{-3}$ and $\hat{v} = 1 \text{ mm}^2/\text{s}$ at $\beta = 75^\circ$ (yellow \blacklozenge), $\beta = 80^\circ$ (black \cdot), $\beta = 70^\circ$ (cyan \blacktriangle); $At = 1.5 \times 10^{-3}$ and $\hat{v} = 1 \text{ mm}^2/\text{s}$ at $\beta = 75^\circ$ (green \blacktriangleleft), $\beta = 80^\circ$ (black \blacksquare), $\beta = 70^\circ$ (magenta \blacktriangleright); $At = 5.5 \times 10^{-3}$, $\beta = 75^\circ$, and $\hat{v} = 1.8 \text{ mm}^2/\text{s}$ (magenta $*$); $At = 10^{-2}$, $\beta = 75^\circ$, and $\hat{v} = 2.5 \text{ mm}^2/\text{s}$ (blue \blacktriangledown). The solid line in panel (b) represents the prediction of the empirical correlation (9). Simulation results in panel (b), described later in the text, are marked by orange \star and correspond to $At = [10^{-2}, 5.5 \times 10^{-3}, 1.5 \times 10^{-3}]$, $\hat{v} = 1 \text{ mm}^2/\text{s}$, and $\beta = 75^\circ$.

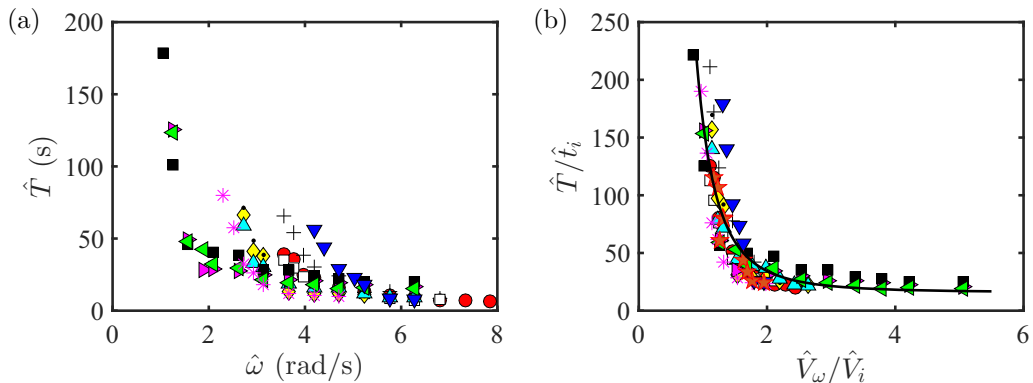


FIG. 11. Variation of the propagation time of the stopping front as a function of the pipe rotation speed plotted in (a) the dimensional plane ($\hat{\omega}$, \hat{T}); (b) the dimensionless plane (\hat{V}_ω/\hat{V}_i , \hat{T}/\hat{t}_i). Different markers are the same as in Fig. 10. The solid line in panel (b) represents the prediction of the empirical correlation (9).

in which for simplicity we take c to be an integer. We find that $a = 10.4$, $b = 48.4$, and $c = -3$, where $a \in (7.8, 13.0)$ and $b \in (42.2, 54.6)$ with confidence level 95%. Lifting the constraint on c would result in $c = -2.8 \in (-3.5, -2.0)$ with confidence level 95%, implying that taking c to be an integer is acceptable. Figure 10(b) shows a comparison of the experimental data with the prediction

$$\frac{\hat{L}}{\hat{R}} \approx 10.4 + 48.4 \left(\frac{\hat{V}_\omega}{\hat{V}_i} \right)^{-3}. \quad (7)$$

It is noted here that there is a relatively small constant value, i.e., 10.4, present in Eq. (7), implying that even at very large rotation speeds, the fluids can interpenetrate over a small distance.

Figure 11 is a supplement to Fig. 10, providing information about the effects of rotation speed on the propagation time when the front nearly stops (\hat{T}). Figure 11(a) shows the variation of \hat{T} versus $\hat{\omega}$. Figure 11(b) shows the variation of \hat{T} normalized to the characteristic inertial-buoyant time scale, i.e., $\hat{t}_i = \hat{R}/\hat{V}_i$, versus \hat{V}_ω/\hat{V}_i , showing a power-law variation, which is similar in its form to the propagation distance and can be obtained as

$$\frac{\hat{T}}{\hat{t}_i} \approx a' + b' \left(\frac{\hat{V}_\omega}{\hat{V}_i} \right)^{c'}, \quad (8)$$

in which for simplicity we take c' to be an integer. We find that $a' = 15.9$, $b' = 148.0$, and $c' = -3$, where $a' \in (9.4, 22.4)$ and $b' \in (132.6, 163.4)$. Lifting the constraint on c' would result in $c' = -2.8 \in (-3.4, -2.2)$ with confidence level 95%, implying that taking c' to be an integer is acceptable. Figure 11(b) shows a comparison of the experimental data with the prediction

$$\frac{\hat{T}}{\hat{t}_i} \approx 15.9 + 148.0 \left(\frac{\hat{V}_\omega}{\hat{V}_i} \right)^{-3}, \quad (9)$$

showing reasonable agreement.

E. Mixing

Figure 12 provides an understanding of the degree of mixing between the fluids, for several sets of experimental parameters. This figure shows the variation of the standard deviation of the normalized concentration field between the gate valve and the front, denoted as σ , versus the dimensionless distance from the gate valve, i.e., \hat{x}/\hat{R} . A standard deviation equal to 0.5 would represent complete segregation between the fluids. As can be seen, all the data points are below 0.5, meaning that there

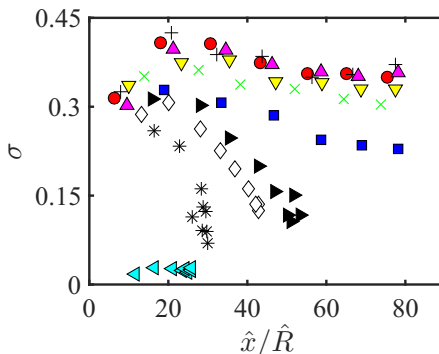


FIG. 12. Variation of the standard deviation of the normalized concentration field between the gate valve and the front, σ , as a function of the dimensionless distance from the gate valve, \hat{x}/\hat{R} , at $\beta = 75^\circ$, $\hat{\nu} = 1 \text{ mm}^2/\text{s}$, $At = 10^{-2}$, and $\hat{\omega} = 0$ (red \bullet), $\hat{\omega} = 0.52$ (black $+$), $\hat{\omega} = 1.57$ (magenta \blacktriangle), $\hat{\omega} = 2.09$ (yellow \blacktriangledown), $\hat{\omega} = 2.62$ (green \times), $\hat{\omega} = 3.14$ (blue \blacksquare), $\hat{\omega} = 3.56$ (black \blacktriangleright), $\hat{\omega} = 3.77$ (black \blacklozenge), $\hat{\omega} = 4.19$ (black $*$), and $\hat{\omega} = 4.71$ (cyan \blacktriangleleft) rad/s. The penetration front stops in fluid flows corresponding to $\hat{\omega} \geq 3.56$ rad/s. The time interval of the adjacent data points is 1.6 s.

is always a degree of mixing between the fluids. At low rotation speeds ($\hat{\omega} = 0$ –2.65 rad/s), the standard deviation remains almost constant as the front propagates along the pipe, and its mean value is close to 0.3–0.4, implying a small mixing. At a moderate value of the pipe rotation speed, i.e., $\hat{\omega} = 3.14$ rad/s, the standard deviation slowly decreases with \hat{x}/\hat{R} and for $\hat{\omega} \geq 3.56$ rad/s a significant drop in σ versus \hat{x}/\hat{R} is observed. For these flows, i.e., $\hat{\omega} \geq 3.56$ rad/s, the front eventually stops before reaching the end of the pipe. As can be seen in Fig. 12, the degree of mixing between the fluids strongly depends on the rotation speed and, as σ decreases, a more enhanced mixing between the fluids is expected to occur.

IV. NUMERICAL RESULTS

The numerical simulations of the exchange flows presented in this paper are implemented and solved using the open-source computational fluid dynamics software OpenFOAM. An overview of the model and the solution procedure is given in the Appendix. Qualitative and quantitative comparisons can be made between the simulation and experimental results, but the simulation results are particularly used to analyze the flow features that are not accessible or observable in the experiments.

Some validations of the numerical simulations against the experimental results can be seen in Figs. 9, 10, and 11, showing reasonable agreement in terms of the variation of the long-time front velocity, the propagation distance, and the propagation time, versus \hat{V}_ω/\hat{V}_i .

For a given set of flow parameters and increasing values of the rotation speed, Fig. 13 illustrates the concentration field in the pipe central planes (both side and top views), showing agreement with the experimental observations, in particular those of Fig. 2. These simulation results also reveal that as the rotation speed increases, the front gradually moves away from the lower wall of the pipe, a feature that cannot be visualized in the experiments. This phenomenon emphasizes the dominance of the rotational inertia over buoyancy in governing the flow dynamics at high rotation speeds. To better illustrate the front shape as $\hat{\omega}$ increases, Fig. 14 presents the isosurfaces at the contraction values equal to 0.5, representing the *pseudointerface* through an axial view of the pipe.

Figure 15 shows the variation of the concentration field, axial velocity contours, and velocity vectors, in the pipe central plane (side view) as well as two pipe cross sections (at $\hat{x} = [0.1, 0.5] \text{ m}$), versus the pipe rotation speeds. It can be seen that as the rotation speed increases, the transverse mixing between the two fluids increases; in fact, at the highest rotation speed, the two fluids are

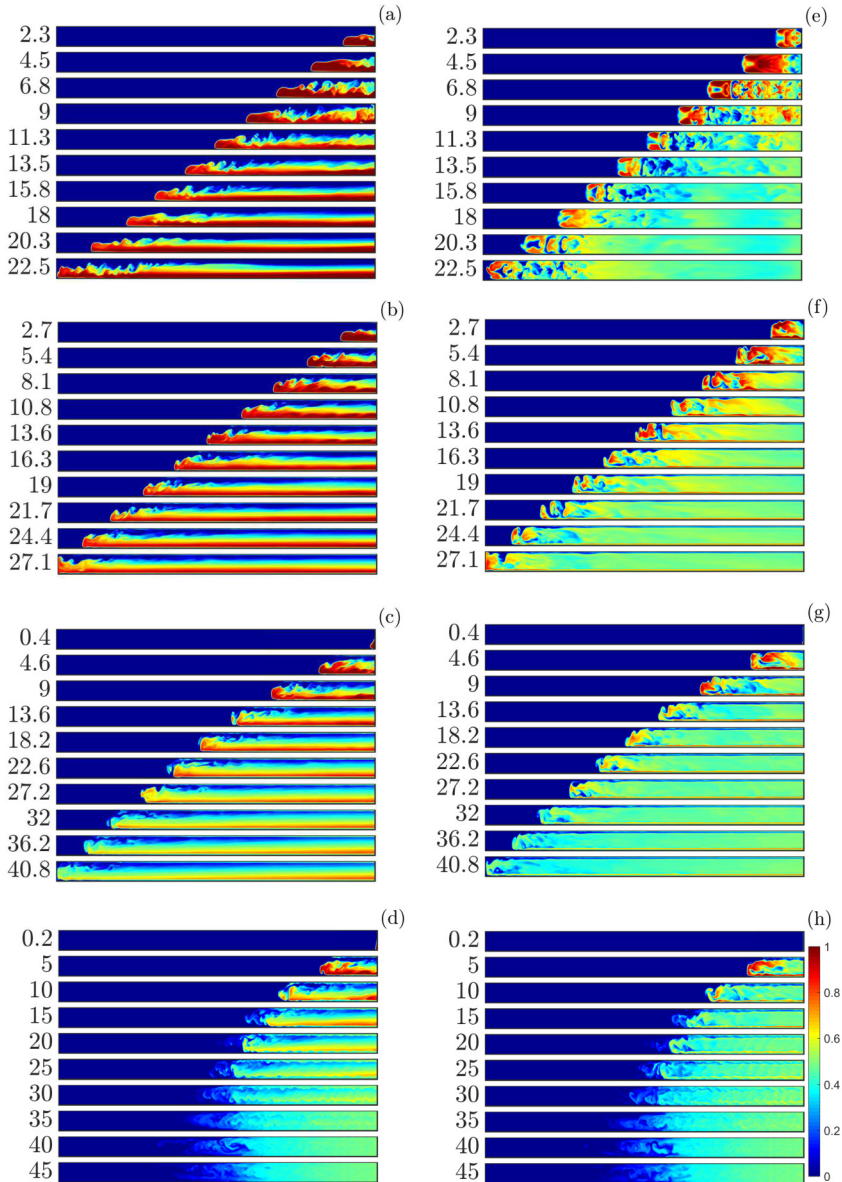


FIG. 13. Numerical simulations corresponding to experimental results in Fig. 2. Image sequences of the concentration field in the pipe central plane: (a)–(d) side view; (e)–(h) top view. The field of view in each snapshot is $19 \times 700 \text{ mm}^2$, below an imaginary gate valve in the simulations. The heavy fluid moves from right to left in each snapshot.

effectively mixed across the pipe diameter. While at low rotation speeds the fluid mixing is finite and constrained within the layer where interfacial instabilities occur, at higher rotation speeds, the effect of the rotational inertia appears to become stronger as the fluid mixing is enhanced; at the highest rotation speed, the flow dynamics is completely dominated by the rotational inertia.

In Fig. 15, the contours of the axial velocity component in the two pipe cross sections at various rotation speeds reveal that the effect of increasing the pipe rotation on suppressing the axial velocity

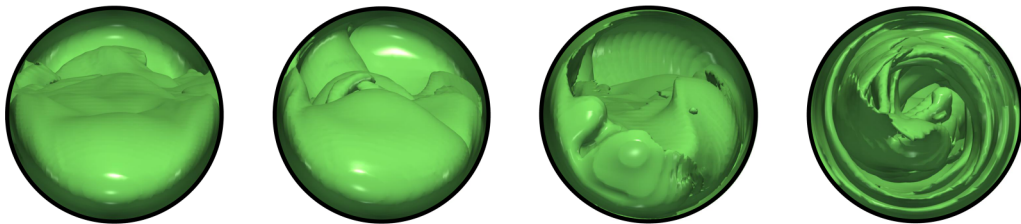


FIG. 14. Numerical isosurface representations at contraction values equal to 0.5 (camera parallel projection view). From left to right, the results correspond to the simulations of Figs. 13(a)–13(d). From left to right, the axial views are captured at $\hat{t} = [18, 21.7, 32, 35]$ s.

is significant and evident. As can be seen in Fig. 15(a), when there is no pipe rotation applied to the fluid exchange system, the front of the heavy fluid penetrates rapidly downward, underneath the light fluid, as the light fluid flow moves upward. The cross-section slices provide insight into the distribution of the maximum axial velocity, revealing that the maximum axial velocity slightly shifts or rotates toward the rotation direction. Finally, the velocity vectors show that by increasing the rotation speed, the axial movements of the fluids are reduced, as the rotation further and further diffuses from the wall toward the pipe center.

V. CONCLUSIONS

In conclusion, an experimental or numerical study is carried out to analyze buoyant miscible exchange flows in an axially rotating pipe, inclined over intermediate inclination angles. The influence of the pipe axial rotation on the dynamics of the flow is investigated. The variation of the penetration front velocity versus the pipe rotation speed is independent of the inclination angle (β) and the common kinematic viscosity of the fluids ($\hat{\nu}$). As the rotation speed ($\hat{\omega}$) increases from zero, the front velocity decreases nonlinearly with $\hat{\omega}$ until it finally becomes zero, at a propagation distance with respect to the initial flat interface between the two fluids. An empirical correlation suitable for predicting the front velocity at long time, \hat{V}_f , is proposed, i.e., $\frac{\hat{V}_f}{\hat{V}_i} \approx 1.07 - 0.24(\frac{\hat{V}_\omega}{\hat{V}_i}) - 0.41(\frac{\hat{V}_\omega}{\hat{V}_i})^2$, where \hat{V}_i and \hat{V}_ω are the characteristic inertial-buoyant and rotational velocities, respectively. In addition, empirical correlations to predict the propagation distance (\hat{L}) and time (\hat{T}) are also found as $\frac{\hat{L}}{\hat{R}} \approx 10.4 + 48.4(\frac{\hat{V}_\omega}{\hat{V}_i})^{-3}$ and $\frac{\hat{T}}{\hat{t}_i} \approx 15.9 + 148.0(\frac{\hat{V}_\omega}{\hat{V}_i})^{-3}$, respectively, where \hat{t}_i is the characteristic inertial-buoyant timescale. A final note is that the correlations offered in this work are purely empirical based on the experimental data; thus, a rigorous theoretical analysis of the flow seems to be appropriate as a future research direction, to bring to light the flow physics behind our buoyancy exchange flows in axially rotating pipes.

ACKNOWLEDGMENTS

This research has been carried out at Université Laval, supported financially by the Fonds de Recherche du Québec–Nature et technologies (via the New University Researchers Start-Up Program) as well as the Canada Foundation for Innovation (through the John R. Evans Leaders Fund). S.L. also appreciates the generous Ph.D. scholarship provided by the China Scholarship Council. The participation of J. Noël, J. N. Ouellet, and M. Lavoie is acknowledged in the construction of the experimental apparatus and useful technical discussions. The computational part of this research has been enabled by support provided by Calcul Quebec and Compute Canada, which is gratefully acknowledged.

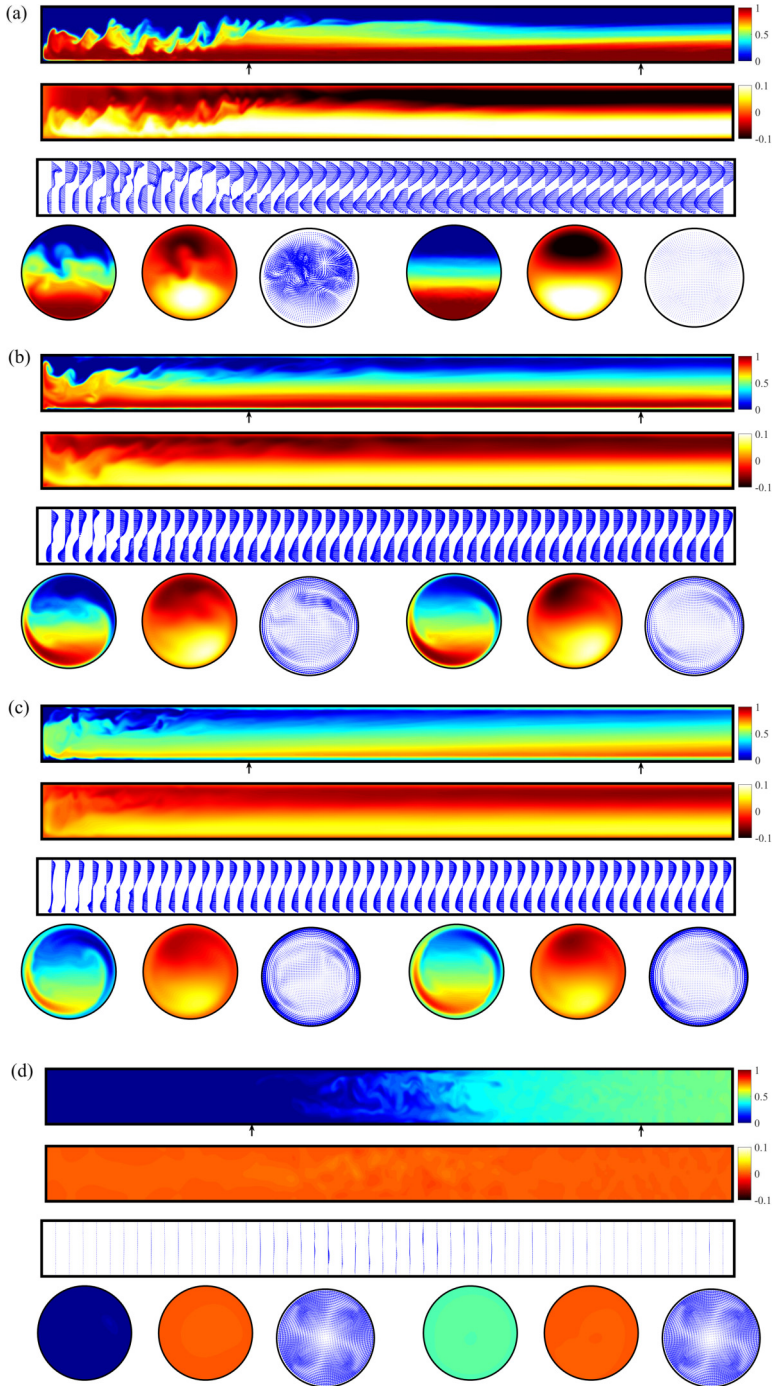


FIG. 15. Numerical simulations with the same parameters as in Figs. 2 and 13. In each panel, the three rectangles show the pipe central plane (side view), with concentration field contours, axial velocity contours, and velocity vectors, from top to bottom, while the circles illustrate these results within the pipe cross section, at $\hat{x} = [0.1, 0.5]$ m marked by the two arrows. The results for panels (a) to (d) correspond to $\hat{t} = [22.5, 27.1, 40.8, 45.0]$ s, respectively. The field of view in the top three images in each panel is 19×700 mm², right below the gate valve.

APPENDIX: COMPUTATIONAL METHOD

In this work, three-dimensional numerical simulations are carried out using OpenFOAM. The configuration, the dimensions, the flow parameters, etc., in the numerical simulations are the same as those in the experiments. The fluids are considered to be incompressible, under an isothermal exchange flow configuration.

Considering c to be the local volume fraction of the heavy fluid, the mixture density can be written as

$$\hat{\rho} = c\hat{\rho}_H + (1 - c)\hat{\rho}_L. \quad (\text{A1})$$

Assuming that the density difference is small and that the molecular diffusivity of the binary system is negligible results in the continuity equation in the form of

$$\nabla \cdot \hat{\mathbf{u}} = 0, \quad (\text{A2})$$

where $\hat{\mathbf{u}}$ is the mass-averaged velocity. Thus, combining Eq. (A1) with the mixture mass balance implies that the governing equation for c is [25]

$$\frac{\partial c}{\partial \hat{t}} + \nabla \cdot (c\hat{\mathbf{u}}) = 0. \quad (\text{A3})$$

The momentum balance equation can be written as

$$\frac{\partial \hat{\mathbf{u}}}{\partial \hat{t}} + \hat{\mathbf{u}} \nabla \cdot \hat{\mathbf{u}} = -\frac{1}{\hat{\rho}} \nabla \hat{p} + \hat{\nu} \nabla \cdot [\nabla \hat{\mathbf{u}} + {}^T \nabla \hat{\mathbf{u}}] + \hat{\mathbf{g}}, \quad (\text{A4})$$

where \hat{t} denotes the time, \hat{p} the pressure, and $\hat{\mathbf{g}}$ the gravity. The governing Eqs. (A2), (A3), and (A4) are discretized and solved using the finite-volume method. An optimized twoLiquidMixingFoam solver with the volume of fluid (VOF) approach [26] is used to simulate the miscible exchange flow, where the volume fraction of each phase is captured and the two fluids are allowed to mix. To set the boundary conditions, the axial rotation velocity is specified at solid boundaries (i.e., no wall slip) and static wall conditions are considered at the pipe inlet and outlet.

Gradient terms are computed using the Gauss linear scheme and, for divergence terms, Gauss linearUpwind grad(U) and Gauss VanLeer are used for velocity flux and phase fraction, respectively. The equations are solved via the PIMPLE algorithm, i.e., combining the pressure-implicit split operator (PISO) and the semi-implicit method for pressure-linked equations (SIMPLE) algorithm, and the GAMG solver. Temporal discretization is also performed via the explicit Euler method. The time step is adjusted according to a maximum Courant number set to 0.5. The structured mesh is generated by the blockMesh utility and for the mesh size a reasonable compromise between accuracy and computing time is achieved for a total of 5.6×10^6 cells. The simulations are run in parallel on a cluster with 80 cores via Calcul Quebec and Compute Canada.

-
- [1] B. D. Maurer, D. T. Bolster, and P. F. Linden, Intrusive gravity currents between two stably stratified fluids, *J. Fluid Mech.* **647**, 53 (2010).
 - [2] Y. Tanino, F. Moisy, and J. P. Hulin, Laminar-turbulent cycles in inclined lock-exchange flows, *Phys. Rev. E* **85**, 066308 (2012).
 - [3] K. U. Kobayashi and R. Kurita, Unstable yet static initial state: A universal method for studying Rayleigh-Taylor instability and lock exchange, *Phys. Rev. Fluids* **4**, 013901 (2019).
 - [4] M. Debacq, V. Fanguet, J. P. Hulin, D. Salin, and B. Perrin, Self-similar concentration profiles in buoyant mixing of miscible fluids in a vertical tube, *Phys. Fluids* **13**, 3097 (2001).
 - [5] M. Debacq, J. P. Hulin, D. Salin, B. Perrin, and E. J. Hinch, Buoyant mixing of miscible fluids of varying viscosities in vertical tubes, *Phys. Fluids* **15**, 3846 (2003).

- [6] F. M. Beckett, H. M. Mader, J. C. Phillips, A. C. Rust, and F. Witham, An experimental study of low-Reynolds-number exchange flow of two Newtonian fluids in a vertical pipe, *J. Fluid Mech.* **682**, 652 (2011).
- [7] T. Séon, J. Znaïen, B. Perrin, E. J. Hinch, D. Salin, and J. P. Hulin, Front dynamics and macroscopic diffusion in buoyant mixing in a tilted tube, *Phys. Fluids* **19**, 125105 (2007).
- [8] Y. Hallez and J. Magnaudet, Buoyancy-induced turbulence in a tilted pipe, *J. Fluid Mech.* **762**, 435 (2015).
- [9] T. Séon, J. Znaïen, D. Salin, J. P. Hulin, E. J. Hinch, and B. Perrin, Transient buoyancy-driven front dynamics in nearly horizontal tubes, *Phys. Fluids* **19**, 123603 (2007).
- [10] S. M. Taghavi, K. Alba, T. Séon, K. Wielage-Burchard, D. M. Martinez, and I. A. Frigaard, Miscible displacement flows in near-horizontal ducts at low Atwood number, *J. Fluid Mech.* **696**, 175 (2012).
- [11] T. Séon, J. P. Hulin, D. Salin, B. Perrin, and E. J. Hinch, Buoyancy driven miscible front dynamics in tilted tubes, *Phys. Fluids* **17**, 031702 (2005).
- [12] T. J. Pedley, On the instability of viscous flow in a rapidly rotating pipe, *J. Fluid Mech.* **35**, 97 (1969).
- [13] P. A. Mackrodt, Stability of Hagen-Poiseuille flow with superimposed rigid rotation, *J. Fluid Mech.* **73**, 153 (1976).
- [14] S. Wang, Z. Rusak, R. Gong, and F. Liu, On the three-dimensional stability of a solid-body rotation flow in a finite-length rotating pipe, *J. Fluid Mech.* **797**, 284 (2016).
- [15] K. Shrestha, L. Parras, C. Del Pino, E. Sanmiguel-Rojas, and R. Fernandez-Feria, Experimental evidence of convective and absolute instabilities in rotating Hagen-Poiseuille flow, *J. Fluid Mech.* **716**, R12 (2013).
- [16] A. Miranda-Barea, C. Fabrellas-García, L. Parras, and C. del Pino, Hydrodynamic instabilities in the developing region of an axially rotating pipe flow, *Fluid Dyn. Res.* **47**, 035514 (2015).
- [17] K. A. Baldwin, M. M. Scase, and R. J. A. Hill, The inhibition of the Rayleigh-Taylor instability by rotation, *Sci. Rep.* **5**, 11706 (2015).
- [18] M. Carrasco-Teja and I. A. Frigaard, Displacement flows in horizontal, narrow, eccentric annuli with a moving inner cylinder, *Phys. Fluids* **21**, 073102 (2009).
- [19] S. Lyu and S. M. Taghavi, Stratified flows in axially rotating pipes, *Phys. Rev. Fluids* **3**, 074003 (2018).
- [20] B. Brunone and A. Berni, Wall shear stress in transient turbulent pipe flow by local velocity measurement, *J. Hydraul. Eng.* **136**, 716 (2010).
- [21] M. M. Scase, K. A. Baldwin, and R. J. A. Hill, Rotating Rayleigh-Taylor instability, *Phys. Rev. Fluids* **2**, 024801 (2017).
- [22] G. I. Taylor, Motion of solids in fluids when the flow is not irrotational, *Proc. R. Soc. London, Ser. A* **93**, 99 (1917).
- [23] J. J. Kuehl and V. A. Sheremet, Two-layer gap-leaping oceanic boundary currents: Experimental investigation, *J. Fluid Mech.* **740**, 97 (2014).
- [24] J. Proudman, On the motion of solids in a liquid possessing vorticity, *Proc. R. Soc. London, Ser. A* **92**, 408 (1916).
- [25] Y. Hallez and J. Magnaudet, Effects of channel geometry on buoyancy-driven mixing, *Phys. Fluids* **20**, 053306 (2008).
- [26] A. Etrati and I. A. Frigaard, Viscosity effects in density-stable miscible displacement flows: Experiments and simulations, *Phys. Fluids* **30**, 123104 (2018).